Poly(vinylidene fluoride)–Acrylic Rubber Partially Miscible Blends: Phase Behavior and Its Effects on the Mechanical Properties

Mohammad Mahdi Abolhasani,[1] Qipeng Guo,[2] Azam Jalali-Arani,[1] Hossein Nazockdast[1]

[1]Department of Polymer Engineering and Color Technology, Amirkabir University of Technology, Tehran, Iran
[2]Polymers Research Group, Institute for Frontier Materials, Deakin University, Locked Bag 2000, Geelong, Victoria 3220, Australia
Correspondence to: A. Jalali-Arani (E - mail: ajalali@aut.ac.ir)

ABSTRACT: A phase diagram of poly(vinylidene fluoride) (PVDF) and acrylic rubber (ACM) was plotted, and the effects of the extent of miscibility on the mechanical properties of the polymer blends were examined. A compressible, regular solution model was used to forecast the phase diagram of this blend. The model prediction, the lower critical solution temperature (LCST) over the upper critical solution temperature (UCST), was done qualitatively according to the experimentally determined phase diagram by differential scanning calorimetry (DSC), optical microscopy, and rheological analysis. These experimental methods showed that this system was miscible in ACM-rich blends (>50% ACM) and partially miscible in PVDF-rich blends. A wide-angle X-ray diffraction study revealed that PVDF/ACM blends such as neat PVDF had a characteristic α-crystalline peak. The partially miscible blends displayed up to 350% elongation at break; this was a significant increment of this parameter compared to that of neat PVDF(20%). However, the miscible blends showed elongation of up to 1000% [again, a remarkable increase compared to chemically crosslinked ACM (220%)] and displayed excellent mechanical properties and tensile strength and a large elongation at break. For the miscible and partially miscible blends, two different mechanisms were responsible for this improvement in the mechanical properties. It was suggested that in the partially miscible blends, the rubbery depletion layer between the spherulite and the conventional rubber cavitations mechanism were responsible for the increase in the elongation at break, whereas for the miscible blends, the PVDF spherulite acted as a crosslinking junction. The stretched part of the tensile samples in the partially miscible blends showed characteristic β-crystalline peaks in the Fourier transform infrared spectra, whereas that in the miscible blends showed α-crystalline peaks. © 2013 Wiley Periodicals, Inc. J. Appl. Polym. Sci. 000: 000–000, 2013

INTRODUCTION

It is well known that poly(vinylidene fluoride) (PVDF) is miscible with polymers containing carbonyl group, such as polyacrylates,[1–3] polyacetates,[4,5] and polyketones,[6] through the specific interactions of CF_2 dipoles with carbonyl groups. The miscibility of PVDF with poly(methyl methacrylate) (PMMA) has been investigated widely.[7–11] The results of these studies have indicated that the blend of PVDF and PMMA exhibits LCST-type behavior. The PVDF crystallinity decreases with increasing PMMA content, and blends with more than 50% PMMA are amorphous. Recently, it has been shown that PVDF is partially miscible with acrylic rubber (ACM) in blends with more than 50% PVDF and is miscible in ACM-rich blends.[12,13]

The thermodynamics of polymer mixtures and blends were first examined by Flory and Huggins.[14–17] They derived the Flory–

Huggins theory within a rigid lattice frame work. This theory assumes incompressibility for the system and, therefore, imposes some limitations on the model, that is, a failure to forecast the LCST. Hence, researchers have tried to develop theoretical treatments extending the classical Flory–Huggins theory to account for compressibility. Ruzette and Mayes[18] recently derived a simple model for the free energy of mixing (Δg_{mix}) of weakly interacting polymer blends that extends the classical Flory–Huggins model to account for the thermal expansion to insert the compressibility into the regular solution model.[18–20] They claimed, although other compressible models had been developed before, that Mayes theory has the ability to predict the phase behavior for weakly interacting polymer pairs with only the pure-component properties, and it has been used for the prediction of phase behavior of many polymer mixtures.[18–20]

DSC has been used to assess the phase-separation temperature of various blends.[21–23] In this method, upon heating, an exothermic heat flow shift is observed, and its onset is related to the liquid–liquid phase separation.

Rheological techniques also allow one to determine the phase-separation temperature as long as the two components show different viscoelastic and glass-transition temperatures (T_g's).[22,24–31] It is well known that an LCST phase diagram can be precisely identified from rheological measurements through the dynamic temperature ramp of the storage modulus (G'), loss modulus (G''), and complex viscosity. These viscoelastic functions are changed intensely at the demixing temperature; that is, sudden changes in the slopes of these functions at the binodal temperature can be discerned and increase with increasing change in the T_g values of the components.

The toughening of semicrystalline polymers by their blending with rubbers has been investigated widely. Much attention has been paid to investigating the association between the morphology and mechanical properties of these blends, and it has been well established that the dispersed elastomer size has a crucial role in toughening the blends.[32–35] It was reported that droplets with diameters of hundreds of nanometer up to 1 or 2 μm interact with the stress tip at the crack tip and dissipate the energy.

Unfortunately, miscible polymer blends usually exhibit an average of the properties of their individual components; thus, their versatility is limited. Furthermore, like any other single-phase resin, for most applications, single-phase polymer blends need to be reinforced or toughened. Recently, some researchers have claimed that the presence of a crystalline phase in a miscible blend can act as a physical crosslinker.[12,36–39]

In our previous study,[13] we investigated the effects of partial miscibility on the crystalline structure of PVDF/ACM blends. The preliminary results indicated that PVDF and ACM were miscible in ACM-rich blends and partially miscible in blends with more than 50% PVDF. The overall goal of this study was to carefully establish a phase diagram with different techniques and relate the measured mechanical properties to the observed morphology with the phase diagram. This may lead to a new strategy in which the adjustment of the processing condition leads to the desired phase diagram and, consequently, results in the optimized mechanical properties.

EXPERIMENTAL

Materials and Sample Preparation

PVDF [Kynar 710, weight-average molecular weight (M_w) = 70,000, M_w/number-average molecular weight (M_n) = 2, Arkema, Paris, France] and ACM (grade AR71, M_w = 620,000, M_w/M_n = 9, Zeon Advanced Polymix Co., Rayong, Thailand) were used in this study. The major component of the ACM was poly(ethyl acrylate) (PEA), which contained a minor amount (5 wt %) of a chlorine cure-site monomer. All of the polymers were dried in a vacuum oven at 80°C for at least 12 h before processing. The blends with different compositions (a PVDF/ACM % w/w nomenclature is used in the text for the blends) were prepared with a Brabender-type plastic mixer with two rotors at a rotation speed of 100 rpm at 190°C for 10 min. The

samples then were hot-pressed at 200°C into a film with thickness of 200 μm and allowed to slowly cool to room temperature.

We prepared the chemically crosslinked ACM samples by first mixing ACM with sulfur (1 phr), sodium stearate (10 phr), and magnesium oxide (2 phr) in a two-roll mill and then curing the mixtures at 180°C for 1 h under pressure.

Characterization

Dynamic mechanical analysis was carried out with a TA Instruments Q800 (UK) in the tensile mode. The dynamic G' and G'' versus temperature were determined at a frequency of 1 Hz and a heating rate of 3°C/min.

DSC was done with a TA Instrument Q200. To measure the equilibrium melting temperature (T_m^{eq}), neat PVDF and the blends with more than 60% PVDF were melted at 210°C for 10 min, and the miscible blends were melted at a temperature 10°C lower than their phase-separation temperature for 40 min. Then each sample was cooled down to the desired isothermal temperature and maintained at that temperature until the degree of crystallinity did not increase any more. After the completion of isothermal crystallization, the sample was subsequently reheated to 210°C at a rate of 20°C/min to obtain the melting endotherm curve. The DSC technique was also used for phase-separation detection. As the prepared samples were heated at different rates to 210°C, there was a sudden heat capacity shift because of the heat exchange during the phase-separation process. The demixing temperature was determined from the first heating run for all of the samples. All of the samples were prepared with the same thermal history; therefore, the data obtained from the first heating run was not affected by the difference in the thermal history of the sample.

Rheomechanical spectroscopy (RMS) were performed with a stress–strain-controlled rheometer (MCR300, Physica Anton Paar Germany) equipped with disk-type parallel plates 25 mm in diameter and with a 1-mm gap. All of the experiments were carried out under a continuous flow of nitrogen gas around the sample pan. An isochronal dynamic temperature sweep was carried out by the measurement of G' and G'' at a fixed frequency of 0.05 Hz, a certain strain (1%), and a uniform rate of heating (1°C/min) from the homogeneous to the phase-separated regime to detect the onset of the phase separation.

Fourier transform infrared (FTIR) spectroscopy was done with a Bruker 70 instrument (USA) equipped with an attenuated total reflectance unit. For each sample, 64 scans between 500 and 1500 cm^{-1} with a resolution of 4 cm^{-1} were collected.

X-ray diffraction measurement was performed on a Panalytical XRD instrument (Netherlands). The data were recorded in the range $2\theta = 5$–$40°$. All of the samples were scanned continuously with a 0.5° scanning step and a 1-s scanning time.

Small-angle X-ray scattering (SAXS) experiments were conducted at the Australian Synchrotron on the small/wide-angle X-ray scattering beamline with an undulator source, which allowed measurement at a very high flux to moderate scattering angles (θs) and a good flux at the minimum scattering vector

(**q**) limit (0.012 nm^{-1}). The intensity profiles were interpreted as the plot of the scattering intensity (I) versus **q**:

$$\mathbf{q} = (4/\lambda)\sin(\theta/2)$$

where λ is the wavelength and is equal to 0.062 nm.

Optical microscopy (OM) was carried out with two polarizing microscopes (a Nikon Eclipse 80i; USA and an Olympus BX51M; USA) equipped with charge-coupled device cameras under the cross-polarization state.

Scanning electron microscopy (SEM) was done with a Leica S440 instrument (Germany). The samples were cryogenically fractured in liquid nitrogen and then sputter-coated with a thin layer of gold.

The tensile behavior of the blends was analyzed with a Lloyd LR 30 K testing machine (UK) in tensile mode with a load cell with a capacity of 100 N and a gauge length of 10 mm. The specimen was a thin rectangular strip ($25 \times 5 \times 0.2$ mm^3). The stress–strain curves of the samples were obtained at room temperature at a strain rate of 5 mm/min at 75% relative humidity and at a temperature of 20°C. The experiments were repeated with five samples of each composition.

RESULTS AND DISCUSSION

Miscibility

It is known that when two polymers are miscible in the amorphous phase, they show a single T_g. Although the appearance of two T_g's corresponding to an individual phase is a characteristic of immiscibility, the T_g's for a partially miscible blend shift toward each other.

Figure 1 shows the tan δ versus temperature curves for the pure polymers and PVDF/ACM blends. For the blends with more than 50% ACM, only one T_g was visible; this suggested miscibility between the amorphous phase of PVDF with ACM. For blends with less than 50% ACM, the T_g's shifted toward each other and indicated the partial miscibility of the phases in these compositions. This observation was in a good agreement with the results of Li et al.[12]

Figure 2 displays the SEM images of the 80/20, 60/40, and 20/80 blends. The 20/80 and 60/40 blends showed matrix-disperse and cocontinuous morphological characteristic of immiscible blends, whereas the 20/80 blend demonstrated a smooth surface without any inhomogeneities; this indicated the miscibility of the phases at this blend ratio.

The extent of the melting temperature (T_m) depression is a well-known measure of miscibility. So, in the following text, this method is explored for the PVDF/ACM blends.

Nishi and Wang[7] derived the following equation to relate the T_m depression of a crystalline polymer blended with an amorphous polymer to the Flory–Huggins interaction parameter (χ):

$$\left(\frac{1}{T_{mB}^{\text{eq}}} - \frac{1}{T_m^{\text{eq}}}\right) = \frac{-Rv_2}{v_2\Delta H_2}[\chi(1-\phi_2)^2] \quad (1)$$

where T_{mB}^{eq} and T_m^{eq} are the equilibrium melting points of the blend and the homopolymer, respectively; R is the gas constant;
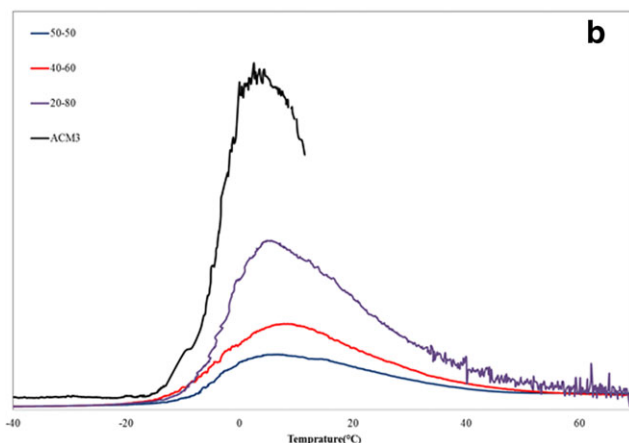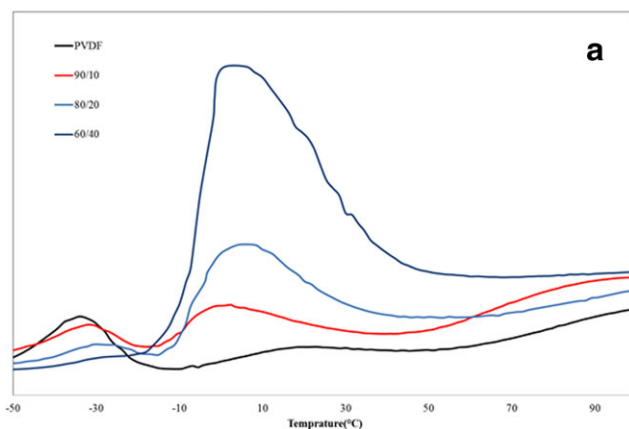

Figure 1. Tan δ versus temperature for the neat PVDF, ACM, (a) immiscible PVDF/ACM blends, and (b) miscible PVDF/ACM blends. [Color figure can be viewed in the online issue, which is available at wileyonlinelibrary.com.]

ΔH_2 is the heat of fusion for the 100% crystalline homopolymer; v_1 and v_2 are the molar volumes of the repeat units of the noncrystallizable and crystallizable components, respectively; and ϕ_2 is the volume fraction of the crystallizable polymer. If the entropic contribution to χ is ignored

$$\chi = \frac{Bv_1}{RT} \quad (2)$$

where B is the interaction energy density and T is the temperature. The combination and rearrangement of eqs. (1) and (2) yields the following:

$$1 - \frac{T_{mB}^{\text{eq}}}{T_m^{\text{eq}}} = \frac{-Bv_2}{\Delta H_2}(\phi_2)^2 \quad (3)$$

where ϕ_1 is the volume fraction of the amorphous polymer.

To obtain the T_m^{eq} values, PVDF T_m's measured by DSC were plotted versus the crystallization temperature (T_c) and extrapolated to the line where T_m was equal to T_c (Figure 3). For the partially miscible blends with increasing T_c, there was no specific trend in the measured T_m values, but for miscible blends in the range of T_c's examined, T_m increased linearly with T_c.
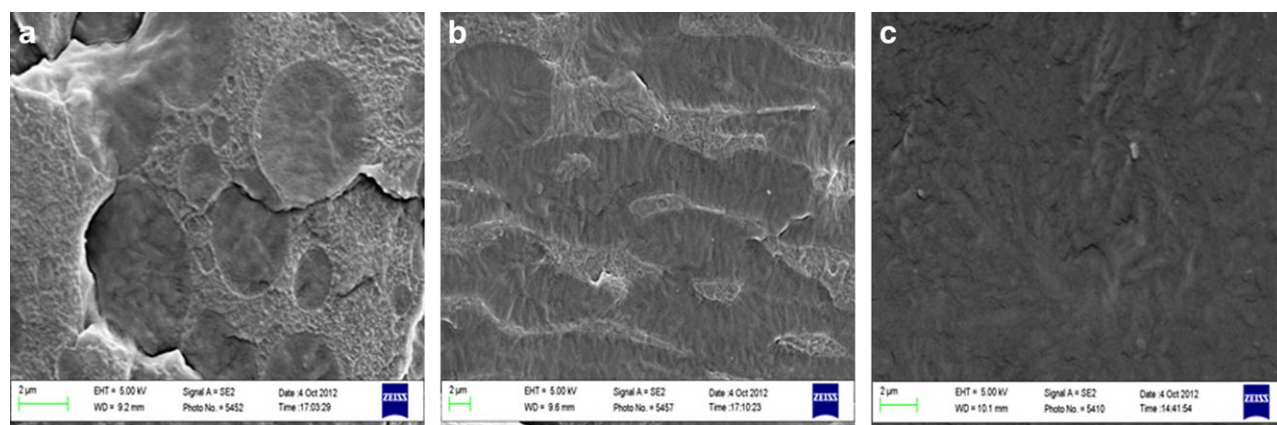
Figure 2. SEM images of the (a) 80/20, (b) 60/40, and (c) 20/80 blends. [Color figure can be viewed in the online issue, which is available at wileyonlinelibrary.com.]

These data could be fitted well to the Hoffman–Weeks equation:[39]

$$T'_m = \phi T_c + (1 - \phi) T_m^{eq} \qquad (4)$$

where T'_m is the melting point and $\phi = 1/\gamma$ is the stability parameter, which depends on the crystal thickness, and γ is the ratio of the lamellar thickness to the initial lamellar thickness (l^*) at T_c. In eq. (4), ϕ varies between 0 and 1. A value of ϕ of 0 suggests that T'_m is equal to T_m^{eq}, whereas a value of ϕ of 1 suggests that T'_m is equal to T_c. Therefore, the most stable crystals are at $\phi = 0$, and the most intrinsically unstable crystals are at $\phi = 1$. There was no noticeable difference in the ϕ values of PVDF and the blends ($\phi \cong 0.24$).

The value of T_m^{eq} obtained for neat PVDF was 174°C, which satisfactorily correlated with the values reported in the literature. Lee and Kim[40] recently found a T_m^{eq} value for PVDF of 173°C. Morra and Stein[10] reported a value of 201°C, and Briber and Khoury[41] presented a value of 184°C. Sencadas et al.[42] stated a value of 190°C. It was previously claimed[10] that the difference in T_m^{eq} seemingly depends on the head-to-head defect content of the polymer.

Figure 4 shows the plot of $1 - T_{mB}^{eq}/T_m^{eq}$ versus $v_2\phi_1^2/\Delta H_2$. From the slope of this curve, a value of $B = -2$ cal/cm^3 was obtained.

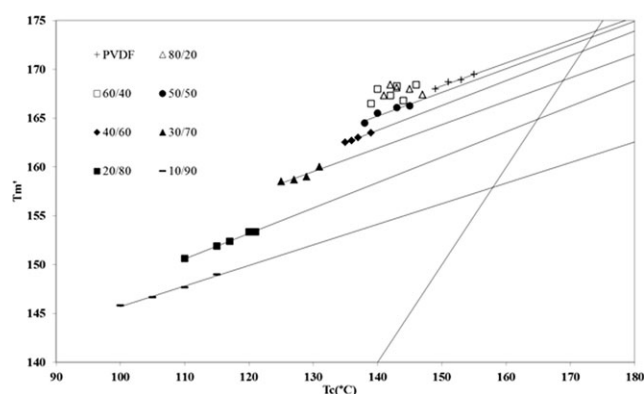This corresponded to a value of $\chi = -0.18$ at 170°C (with an assumed $v_1 = 90.9$ cm3/mol[43]). This value was lower compared to the values reported for PVDF/PMMA and PVDF/PEMA blends of $B = -4.43$ and -2.66 cal/cm^3 respectively.[44] This may have been associated with a lower concentration of carbonyl groups in ACM compared to those in PMMA and PEMA.

Phase Diagram
Prediction. At first, before the phase diagram for the PVDF/ACM blends was plotted, we tried to predict the phase behavior of this blend by a newly introduced compressible, regular solution model. Mayes proposed the following equation for Δg_{mix} per unit volume for A and B components:

$$\Delta g_{mix} = KT \left[\frac{\phi_A \rho_A}{N_A V_A} \ln\phi_A + \frac{\phi_B \rho_B}{N_B V_B} \ln\phi_B \right] \\ + \phi_A \phi_B \rho_A \rho_B (\delta_{A,0} - \delta_{B,0})^2 + \phi_A \phi_B (\tilde{\rho}_A - \tilde{\rho}_B)(\delta_A^2 - \delta_B^2) \qquad (5)$$

where K is the Boltzmann constant, ϕ_i is the volume fraction, and N_i is the number of segments of volume V_i at 0k. $\tilde{\rho} = \rho_i/\rho_i^*$, where ρ_i is the mass density and ρ_i^* is the hardcore density at 0 K. $\delta_{i,0}$ is the hardcore solubility parameter, and δ_i is a temperature- and pressure-dependent solubility parameter.
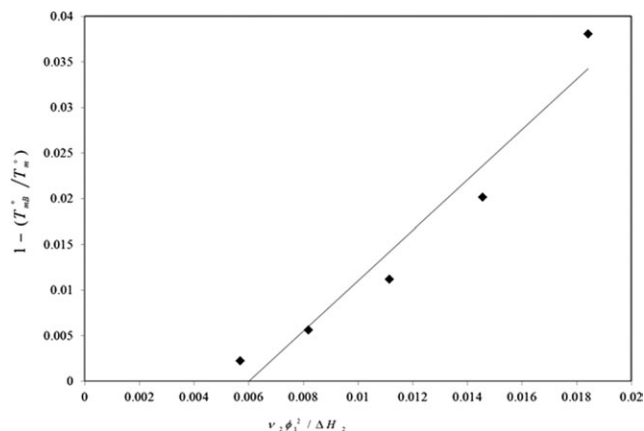

Figure 3. Plots of the observed melting temperature (T_m') versus T_c.

Figure 4. Plot of $(1 - T_{mB}^{eq}/T_m^{eq})$ versus $v_2\phi_1/\Delta H_2$ used to obtain χ.

Table I. Parameters Used for Spinodal Prediction

Polymer	ρ^* (g/cm^3)	α (K^{-1})	$\delta(298)$ (J$^{1/2}$/cm$^{3/2}$)	v (molar volume) (cm^3/mol)
PVDF	1.81	3.6×10^{-5} [a]	15.37[b]	[a]90.9
ACM	1.65	7.2×10^{-4} [c]	19.18[b]	[d]35.95

[a]Obtained from the supplier.
[b]Obtained from a group contribution calculation.[45]
[c]PEA thermal expansion.[1]
[d]Obtained from Ref. 43.

When the second derivative of eq. (5) is taken with respect to the composition, at constant temperature and pressure this yields a spinodal criterion ($g_{\phi\phi}$):

$$g_{\phi\phi} = \frac{\partial^2 \Delta g_{\text{mix}}}{\partial \phi_A^2}\bigg|_{\text{T.P}} \approx \frac{\partial^2 \Delta g_{\text{mix}}}{\partial \phi_A^2}\bigg|_{\text{T.P}.\tilde{\rho}}$$

$$= KT\left[\frac{\tilde{\rho}_A}{\phi_A N_A V_A} + \frac{\tilde{\rho}_B}{\phi_B N_B V_B}\right] - 2\tilde{\rho}_A\tilde{\rho}_B(\delta_{A,0} - \delta_{B,0})^2 \quad (6)$$

$$- 2(\tilde{\rho}_A - \tilde{\rho}_B)(\delta_A^2 - \delta_B^2) > 0$$

The reduced densities were obtained by the Tait equation (empirical) with the assumption of a constant thermal expansion (α_i) value:

$$\rho_i(T) = \rho_i^* \exp(-\alpha_i T) \quad (7)$$

This yields ρ_i^* and hence V_i, the hard core segmental volume, as well as $\tilde{\rho}_i = \rho/\rho_i^*$. $\delta_i(T)$, estimated by extrapolations from the group contribution values of δ_i(298) calculated according to Van Krevelen[45] at 25°C, was extrapolated to other temperatures in the following manner:

$$\delta_i^2(T) = \delta_i^2(298)\left[\frac{\tilde{\rho}_i(T)}{\tilde{\rho}_i(298)}\right] \quad (8)$$

The PVDF and ACM values of α_i, ρ_i^*, δ_i(298), and V_i that were used to compute the spinodal diagrams are listed in Table I.

Figure 5(a) shows the predict phase diagram for the PVDF/ACM blends with Mayes theory. As stated by Mayes and coworkers,[18–20] the primary goal of this theory is to qualitatively predict the phase behavior of polymer mixtures and solutions. The models obviously predict the LCST over the UCST and the skewness of the phase diagram toward the PVDF axis so that the critical point is with the 80/20 PVDF/ACM blend. In the next section, this prediction is compared with experimental data obtained by different methods.

Experiment-Results

To plot the phase diagrams of these blends, DSC, RMS, and OM techniques were used. Given the high molecular weight of the polymers, it can take a long time to interpret how chains lead to a structure detectable by classical techniques such as OM. The OM technique was used to determine the turbidity temperature in the time-sweep mode. The hot-stage temperature in each case was kept constant for 1 h, and the temperature at which the first sign of phase separation was observed was indicated as the binodal temperature of the blend.

Figure 6 shows the morphological development with time for the 20/80 blend. The temperature was kept constant at 230°C in
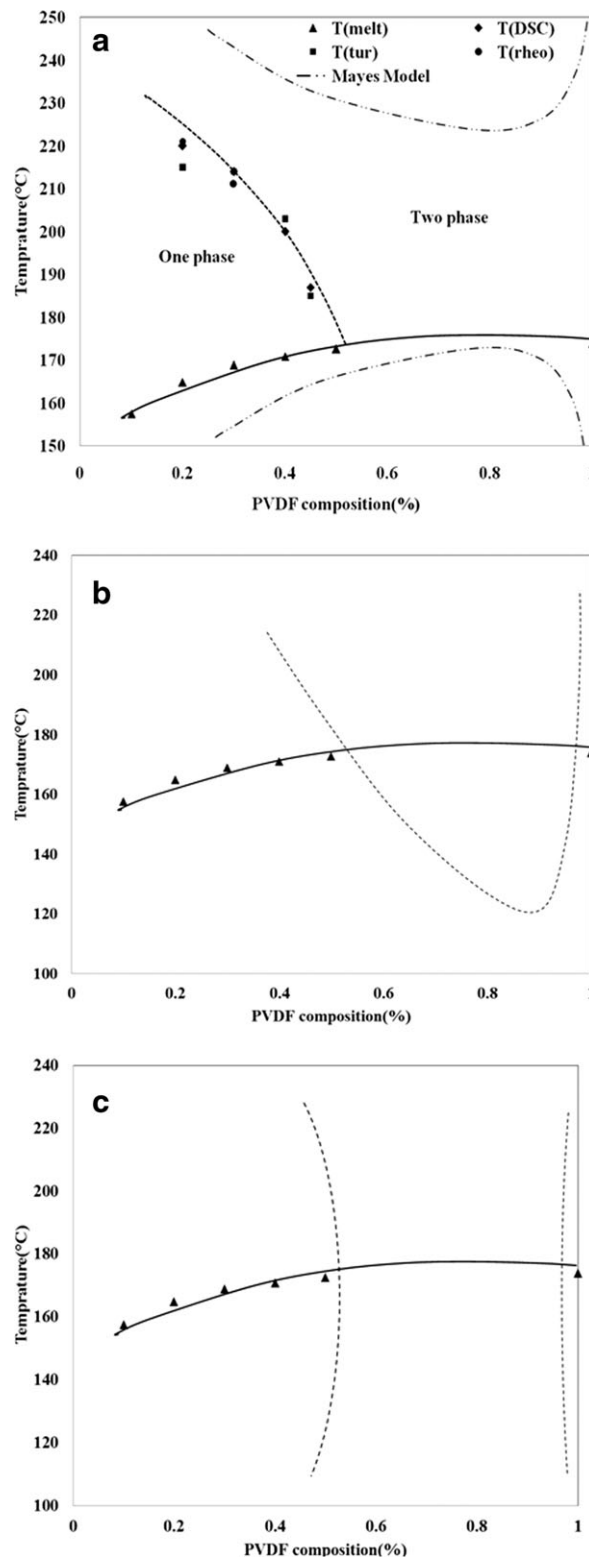

Figure 5. (a) α-PVDF/ACM phase diagram, (b) LCST phase diagram, and (c) hourglass phase diagram; T(melt) is equilibrium melting point temperature, T(tur), T(DSC), and T(rheo) are the phase separated temperature measured by OM, DSC and RMS technique, respectively.

the two-phase region, as depicted in this figure; after 30 min, the transition from a homogeneous structure to a matrix-disperse structure was in its final stage. Figure 6(c) shows the final morphology at higher magnification.

Figure 7(a) shows the DSC thermograms of the 20/80 blend at different heating rates. There was a remarkable shift in the DSC thermogram (T_{DSC}), which was considered the signature of phase demixing. Although the blend was in a miscible state, the PVDF/ACM blend absorbed energy, and there was no sudden heat capacity change in the curve.[21–23] However, in the demixing temperature, there was an energy exchange due to phase-segregation phenomena. In Figure7(b), this temperature was extrapolated to 0°C/min, which was indicative of the binodal temperature; this method was previously used by Ebert et al.[23] for a (PVDF/PMA(poly methyl acrylate)) blend.

Rheological measurement is a reliable method for detecting phase behavior. However, to the best of our knowledge, this is the first time that this method has been used to plot the phase diagram of partially miscible blends.

In Figure 8(a), typical curves of the elastic modulus (G') versus the temperature for the 40/60 and 30/70 blend are shown. In both cases, G' decreased with increasing temperature. This was related to the increment of the chain mobility as the blend moved away from its T_g. In the vicinity of the binodal temperature, there was a competition between the mobility and thermodynamic forces; at the binodal temperature, the thermodynamic forces overwhelmed the mobility and caused a change in the slope of the G' curve through the formation of domains rich in the PVDF component. It has been reported that for blends with large differences in T_g, an upturn in the G' curve is observable, for example, PS/PVME (poly styrene/poly vinyl methyl ether) blends.[22,27] However, for PVDF/ACM blends, as a result of their close T_g's, a smooth change in the slope of the G' curve was observed. This observation was in accordance with ref. 46. The inflection point of the G' versus temperature curve pertained to the rheological binodal temperature (T_{theo}). This definition is empirical and does not establish itself on a physical background. The G'' behavior was similar but had less sensitivity and phase lag. Stress induced by concentration fluctuations had an elastic origin and caused a higher sensitivity in G'. In the analog Maxwell model, the elastic component has a faster and stronger response to a deformation compared to a viscous component.

Spinodal decomposition can be quantitatively estimated by the theoretical approach of Ajji and Choplin,[47] who extended the earlier theoretical treatment of Fredricson and Larson[48] for block copolymer melts near the order–disorder transition. Mean-field theory is used to derive the critical contribution to the shear stress for near-critical polymer mixtures. After the integration over the wave vector (**k**) space, the following expression for the dynamic G' and G'' values is obtainable:

$$G'(\omega) = \frac{k_B T_\omega^2}{15\pi^2} \int_0^{k_c} \frac{k_B \delta_0^2(k)}{\omega^2 + 4\bar{\omega}^2(k)} \left[\frac{\partial \delta_0^{-1}(k)}{\delta k^2}\right]^2 dK \quad (9)$$

$$G''(\omega) = \frac{2k_B T_\omega}{15\pi^2} \int_0^{k_c} \frac{k^6 \delta_0^2(k)\bar{\omega}(k)}{\omega^2 + 4\bar{\omega}^2(k)} \left[\frac{\partial \delta_0^{-1}(k)}{\delta k^2}\right]^2 dK \quad (10)$$

where G' and G'' are storage and loss modulus, respectively. $\bar{\omega}(k) = k^2 S_0^{-1}(k)\lambda(k)$, $S_0(k)$ is the static structure factor, $\lambda(k)$ is the Onsager coefficient, and k is the wave factor.
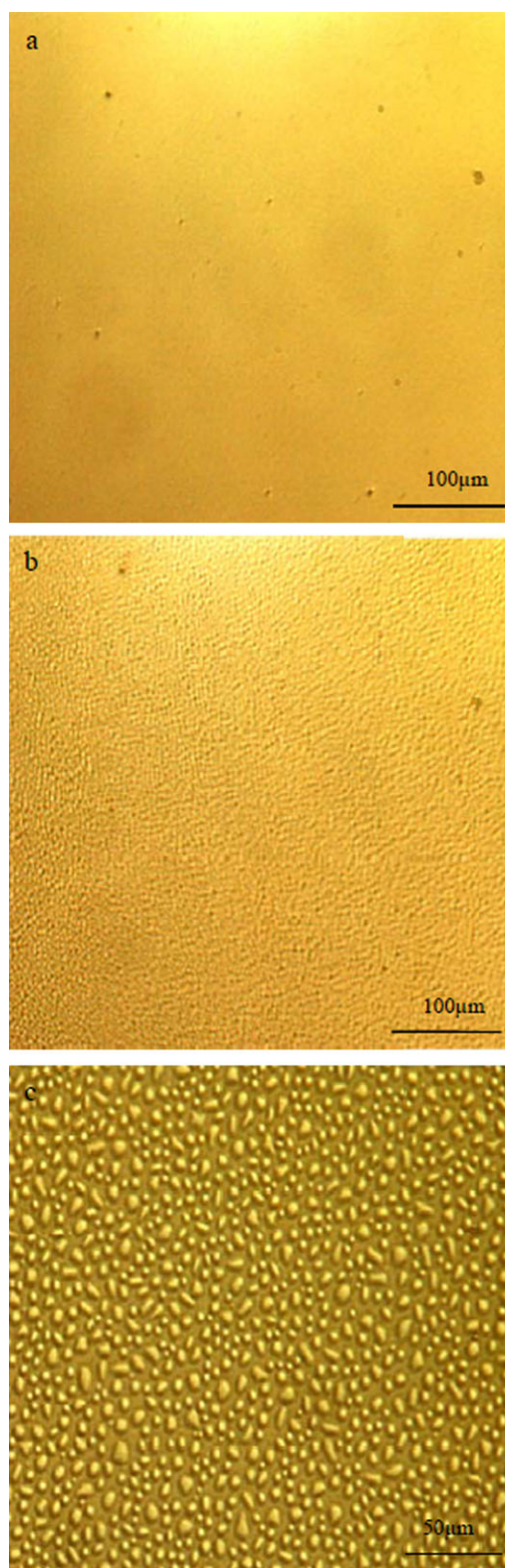

Figure 6. Morphology development by time at 230° C for the 20/80 blend: (a) 0, (b) 15, and (c) 30 min. [Color figure can be viewed in the online issue, which is available at wileyonlinelibrary.com.]
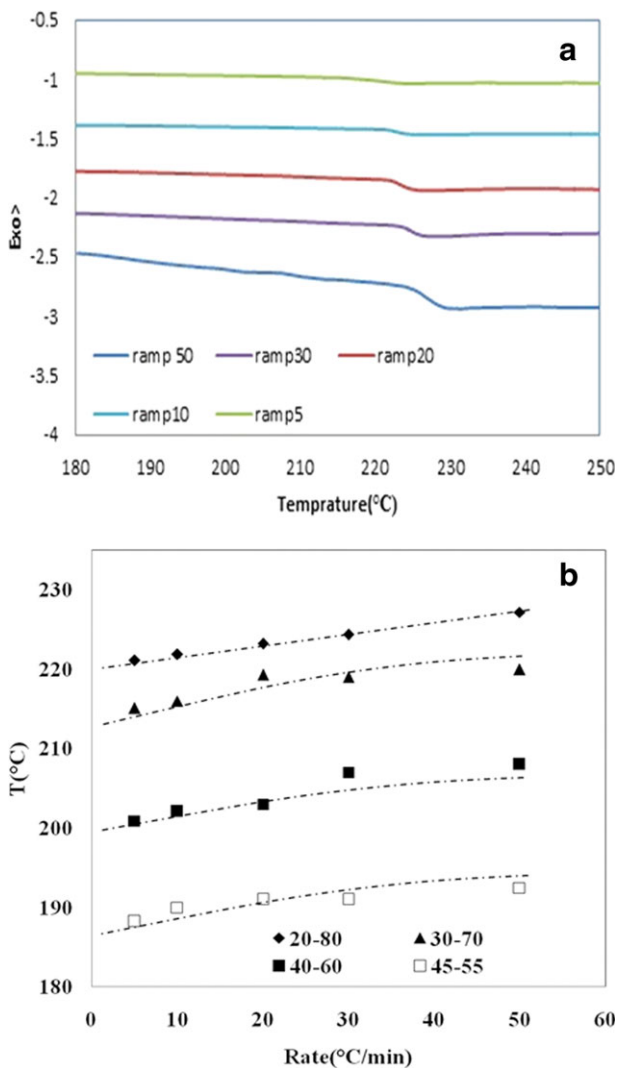
Figure 7. (a) DSC thermograms of the 20–80 blend at different heating rates. (b) T_{DSC} obtained at different heating rates for miscible blends. [Color figure can be viewed in the online issue, which is available at wileyonlinelibrary.com.]

The previous equation could be applied with the De Gennes mean-field structure in the case of binary polymer blends[49]

$$\frac{1}{S_o(k)} = \frac{1}{\phi N_i g_1(k)} + \frac{1}{(1-\phi)N_2 g_2(k)} - 2\chi \quad (11)$$

where N_i is the number of statistical segments and $g_i(k)$ is the Debye function. The expression for the Onsager coefficient $[\lambda(k)]$ is

$$\frac{1}{\lambda(k)} = \frac{1}{\phi b_1^2 W_1 g_1(k)} + \frac{1}{(1-\phi)b_2^2 W_2 g_2(k)} - 2\chi \quad (12)$$

where b_i is the statistical segment length for species i and W_i is the rate of its reorientation and can be defined as follows:
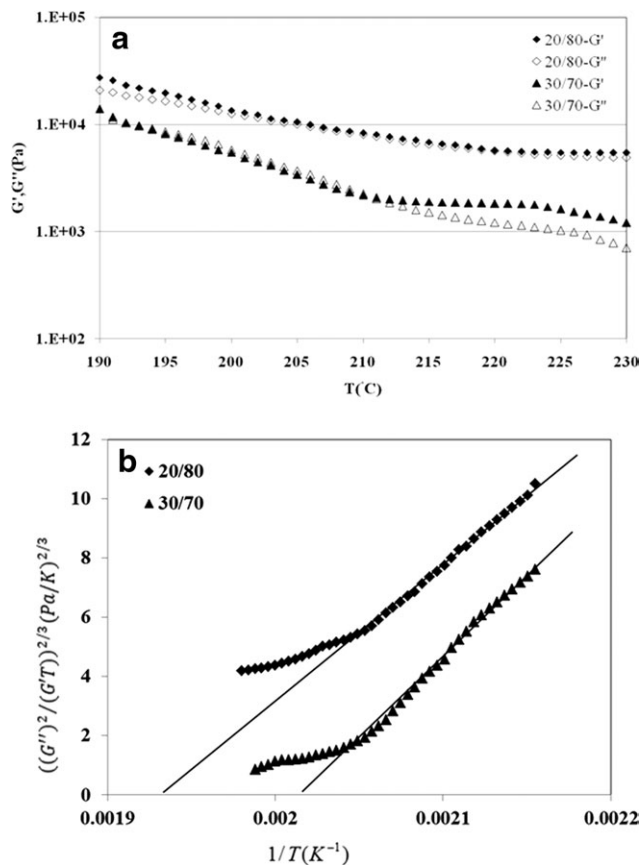
$$W_i = 3\pi k_B T/\xi_i \quad (13)$$

Figure 8. (a) Temperature dependence of the G' and G'' for the 20/80 and 30/70 blends and (b) quantitative evaluation of the viscoelastic behavior of the 20/80 and 30/70 blends near the phase separation and determination of the spinodal temperature.

where ξ_i is the monomeric friction coefficient. For the terminal, one-phase region near the critical point, we have

$$G''(\omega) = \frac{k_B T_\omega}{240\pi} \left[\frac{1}{3}\left\{\frac{Rg_1^2}{\phi N_1} + \frac{Rg_2^2}{(1-\phi)N_2}\right\}\right]^{-1/2}$$
$$\times \left[\frac{1}{\phi b_1^2 W_1} + \frac{1}{(1-\phi)b_2^2 W_2}\right][2(\chi_s - \chi)]^{-1/2} \quad (14)$$

$$G'(\omega) = \frac{k_B T_\omega}{1920\pi} \left[\frac{1}{3}\left\{\frac{Rg_1^2}{\phi N_1} + \frac{Rg_2^2}{(1-\phi)N_2}\right\}\right]^{-1/2}$$
$$\times \left[\frac{1}{\phi b_1^2 W_1} + \frac{1}{(1-\phi)b_2^2 W_2}\right][2(\chi_s - \chi)]^{-5/2} \quad (15)$$

where χ_s is the interaction parameter at the spinodal point. Using the previous equation, one can easily obtain

$$\frac{G'(\omega)}{[G''(\omega)]^2} = \frac{30\pi}{k_B T}\left\{\frac{b_1^2}{36\phi} + \frac{b_2^2}{36(1-\phi)}\right\}^{-3/2}(\chi_s - \chi)^{-3/2} \quad (16)$$

If χ is assumed to equal $A + B/T$, there would be a linear dependence of $[G'(\omega)^2/G''(\omega)T]^{2/3}$ versus $1/T$, for which the interception with the $1/T$ axis is defined as the spinodal temperature.

Table II. Equilibrium melting point and Binodal Point Values

PVDF–ACM	T_m^{eq} (°C)	T_{DSC} (°C)	T_{Tur} (°C)	T_{Rheo}
100/0	174	–	–	–
50/50	173	–	–	–
45/55	–	187	185	–
40/60	171	200	203	–
30/70	169	214	214	212
20/80	165	220	215	221
10/90	158	–	–	–

The experimental results of $[G'(\omega)^2/G'(\omega)T]^{2/3}$ versus $1/T$ for the 40/60 and 30/70 blends are shown in Figure 8(b); a linear range was observable in the phase-transition region, in which the corresponding lines gave an estimate of the spinodal temperature.

Figure 5(a) shows the phase diagram of α-PVDF/ACM plotted with the data presented in Table II. As shown, there was good agreement between the phase-separation temperatures determined by DSC, RMS, and OM. The binodal curve and T_m^{eq} curve intersected at about 173°C and at a composition of 50–60% PVDF. It is worth mentioning that there was no discernible one-phase region in the melt at composition greater than 60% PVDF, and consequently, the binodal curve was skewed to the PVDF-rich side of the phase diagram. The measured phase diagram was determined qualitatively according to the Mayes model prediction. Therefore, this model again showed its ability to correctly predict the phase diagram of this newly introduced blend with the pure polymer properties only.

The other feature of the measured binodal curve was its concave downward shapes; these suggested an hourglass-type phase-separation curve. However, whether the α-PVDF/ACM phase diagram had true LCST behavior [Figure 5(b)] or an hourglass-shaped bimodal behavior [Figure 5(c)] is not really important because the binodal point could not be defined below the T_m curve. Nevertheless, according to the Mayes model prediction, the LCST over the UCST, maybe an hourglass phase behavior was the most probable phase behavior for this blend.

Lamellar Structure and Crystal Forms
Figure 9(a) shows the Lorentz-corrected SAXS profiles of the PVDF/ACM blends and neat PVDF. PVDF showed a scattering peak at $\mathbf{q} = 0.065$ Å^{-1}, which was related to the crystal long period of $L = 9.66$ nm. However, the partially miscible blended show two scattering peaks at $\mathbf{q} = 0.050$ Å^{-1} ($L = 12.56$ nm) and $\mathbf{q} = 0.034$ Å^{-1} ($L = 18.47$ nm), indicative of two type of crystal lamellae coexist in one blend. This observation may originate from partial miscibility of the blends. It can be claimed that crystals with long period of 12.56 nm is related to PVDF crystals in PVDF rich phase, these crystals have only slightly increased long period compare to neat PVDF. Crystals with long period of 18.47 nm comes from PVDF crystals in ACM rich phase. In this case many ACM chains have penetrated to the gallery of PVDF lamella and formed interlamellar structure. On the other hand, miscible blends demonstrate only one scattering peak at $\mathbf{q} = 0.032$ Å^{-1} ($L = 19.63$ nm), indicative of

similar crystal lamellae in miscible blends. This is in agreement with Li et al.[12] observation.

Figure 9(b) displays the wide-angle X-ray diffraction (WAXD) profiles of the neat PVDF and the blends. All of the blends and neat PVDF both revealed typical reflection patterns of α crystals; therefore, blending with ACM had no effect on the crystal form of PVDF.

Mechanical Properties
Partially Miscible Blends. Figure 10(a) shows the stress–strain curves for the PVDF/ACM partially miscible blends and neat PVDF. The neat PVDF was very rigid and brittle and broke at an elongation of about 20%. However, necking occurred for the partially miscible blends. These blends underwent large cold drawing after yielding and then broke at a strain of more than 250%; this was a considerable increment of elongation at break compared to the neat PVDF.

From Figure 2(a), it is obvious that the 80/20 blend had an average droplet size of about 4 μm; this was a bit higher than the value reported for the optimum mechanical properties by the cavitation mechanism, that is, below 1 μm. Therefore, we believe that in addition to the widely used cavitation toughening mechanism, other mechanisms also played an important role in the toughening of these blends. The effects of the
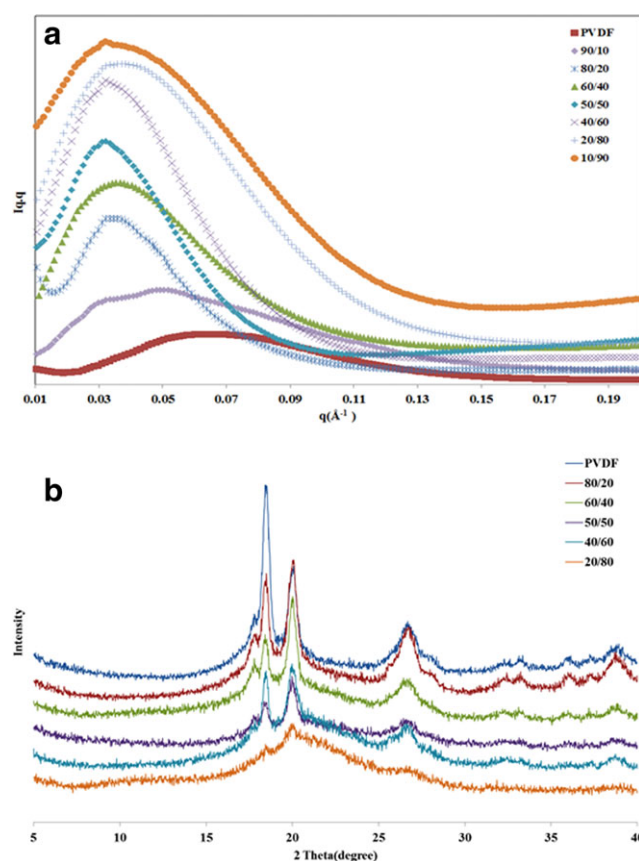

Figure 9. (a) Lorentz-corrected SAXS profiles of the neat PVDF and PVDF/ACM blends and (b) WAXD profiles of the neat PVDF and PVDF/ACM blends. [Color figure can be viewed in the online issue, which is available at wileyonlinelibrary.com.]
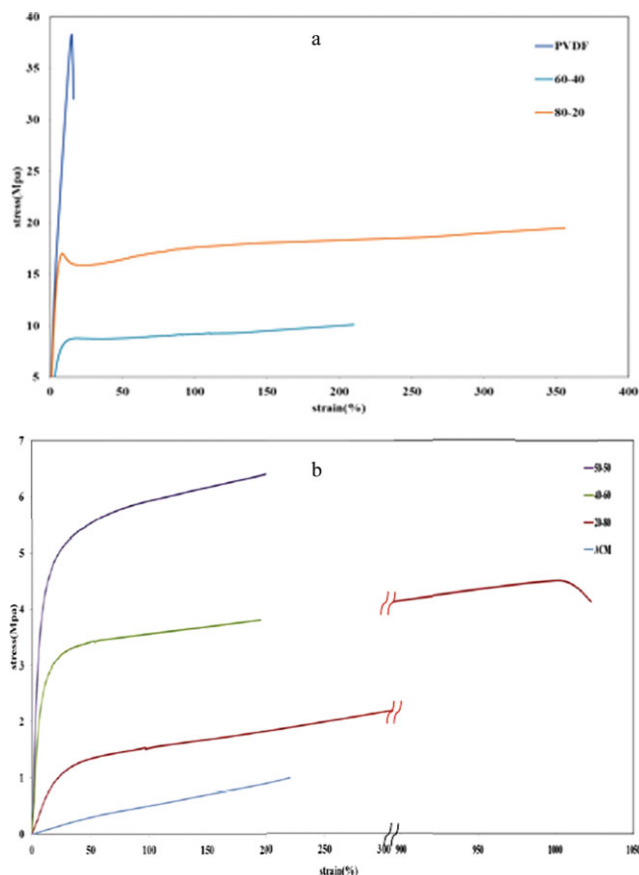
Figure 10. Stress–strain curve for the (a) neat PVDF and immiscible blends and (b) chemically crosslinked ACM and miscible blends (physically crosslinked). [Color figure can be viewed in the online issue, which is available at wileyonlinelibrary.com.]

Figure 11. Presence of the ACM-rich phase inside the spherulites and at the interface of the spherulites. [Color figure can be viewed in the online issue, which is available at wileyonlinelibrary.com.]

decrease in clarity of the yielding phenomena. This behavior was related to the decrease in size of the spherulites with increasing ACM contents, one can easily see in Figure 12.

Miscible Blends

For miscible blends, the situation is completely different. Recently, we showed that blending with ACM in miscible region increases the free energy of folding (σ_e) of PVDF lamella, that is, to 27 erg/cm^2 for neat PVDF and 86 erg/cm^2 for the 20/80 blend.[13] The average of l^* can be determined by the following equation:

$$l^* = \frac{2\sigma_e T_m^{eq}}{\Delta H_f(T_m^{eq} - T_c)} \qquad (17)$$

If l^* divided by φ (stability parameter) obtained by Hoffman-Weeks plot, the later equation for lamellar thickness (L) is obtainable:

$$L = \frac{2\sigma_e T_m^{eq}}{\Delta H_f(T_m^{eq} - T_c)} \times \frac{1}{\varphi} \qquad (18)$$

Where ΔH_f are heat of fusion and crystallization temperature, respectively. From the previous equation, we concluded that an increase in σ_e would cause an increase in L. This observation was in agreement with the SAXS results; therefore, the blending with ACM increased the lamellar thickness, or in other words, the ACM chains diffused into the lamellar gallery of the PVDF spherulite. Then, we could assume that the PVDF spherulites acted as tiny physical crosslinking agents. Such a mechanism has been previously suggested by several authors.[12,36–39] Some researchers modified amorphous polymers by crystalline branches; these branches acted as physical crosslinks tying the amorphous segments in the networks.[36,37] So, an increase in the PVDF content in the miscible blends was considered as an increment in the crosslinking density, which led to lower

spherulite size on the mechanical properties of semicrystalline polymers have been investigated by many authors.[50–52] It has been shown that semicrystalline polymers with small spherulites are tougher than those with large spherulites because coarse spherulites have weaker boundaries. Furthermore, it is believed that the yielding behavior of crystalline polymers is related to the break of large spherulites upon deformation.

Therefore, it seemed that the spherulite size and boundaries were two important factors that, in addition to cavitation, governed the mechanical properties of the PVDF/ACM blends in the partially miscible region. The presence of a depletion layer at the growth front of the spherulite has been reported by many authors.[7,13,41] Figure 11 shows the OM of the 80/20 blend in the phase-contrast mode. The arrays in this figure clearly show the formation of a depletion layer at the boundary of the spherulite, which suppressed the impingement of spherulites and had a significant role in the increment of the elongation at break in the partially miscible blends. In the case of the 60/40 blend, its cocontinuous structure [Figure 2(b)] was the main reason for its lower elongation at break compared to that of the 80/20 blend. The other important feature of Figure 10(a) is the
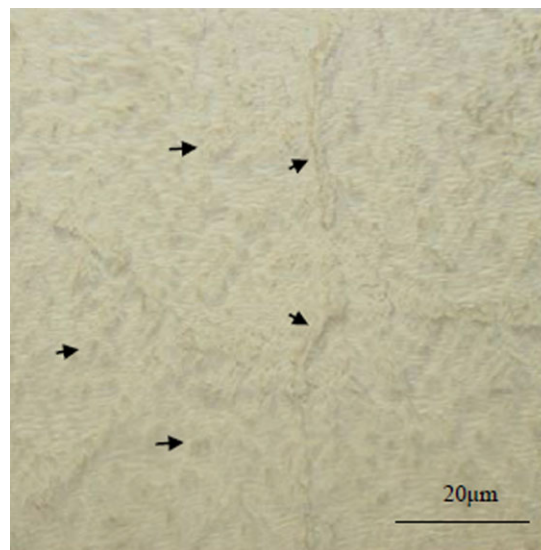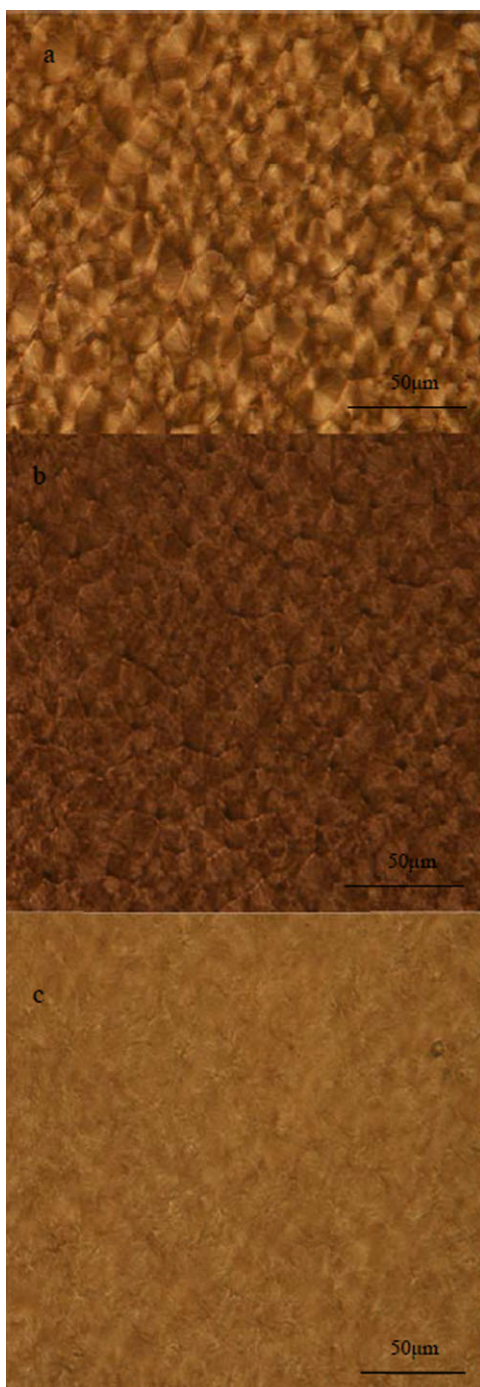
Figure 12. Optical images of the (a) neat PVDF, (b) 80/20 blend, and (c) 20/80 blend. [Color figure can be viewed in the online issue, which is available at wileyonlinelibrary.com.]

elongation at break and higher tensile strength values.[53] In addition, some other authors have suggested a lamellar-to-fibrillar transition at high elongations, such as in the 20/80 blend.[54–56] The other difference in the mechanical properties of the miscible blends versus the partially miscible blends was their yielding behavior. These blends were uniformly elongated with the application of tensile stress. However, in the miscible blends, small and loose spherulites were responsible for suppressing the yielding.
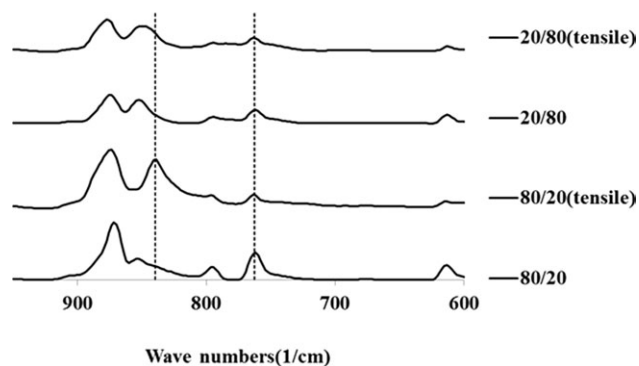

Figure 13. FTIR spectra of the stretched and nonstretched 80/20 and 20/80 blends.

α to β Transition

Figure 13 shows the FTIR–attenuated total reflectance spectra of the stretched films used for tensile testing. Two blends, the 80/20 partially miscible and the 20/80 miscible blends, were chosen to explore the effects of the improvement in mechanical properties on the α to β transition upon stretching at room temperature. We easily observed the appearance of a β polymorph in the stretched 80/20 blend, whereas the 20/80 blend clearly showed the characteristic peak of the α phase and a weak transition to the β phase. It seemed that in the 80/20 blend, most of the α crystals converted to β crystals upon stretching. We believe that this behavior was in complete accordance with the observed mechanical properties. Applied stresses were transferred to the α spherulite and caused α to β transformation in the partially miscible blends, but for the miscible blends, the penetration of ACM chains in the lamellar gallery of the spherulite caused decreases in the number of tie molecules.[54] Therefore, the applied stresses caused the rotation of the crystals in the direction of stress instead of converting α crystals to β crystals.

For the piezoelectric application of PVDF films, because of mechanical restrictions, in which they are usually stretched at 90–100°C to obtain a β polymorph, to our knowledge, this is the first time that α to β transformation upon cold drawing has been reported.

CONCLUSIONS

Polymer blends of PVDF/ACM were prepared by melt mixing. A phase diagram of this blend was plotted by RMS, DSC, and OM techniques. These techniques clearly showed an LCST-type behavior for this blend. The experimentally determined phase diagram was determined qualitatively according to Mayes model prediction. The phase diagram intersected with the T_m^{eq} curve determined by DSC.

The WAXD results showed that upon blending with ACM, no crystal form transition was observed, and the SAXS experiments showed two constituent lamella with long periods of 12.56 and 18.47 nm in the partially miscible blends indicative of dual lamellar crystal coexistence in this system. The blended samples showed superior elongation at break compared to that of neat PVDF. It was suggested that in addition to the common

cavitation mechanism, this improvement was related to the presence of a rubbery ACM depletion layer between the large spherulites of PVDF in the partially miscible sample. However, in the miscible blends, ACM chains penetrated the gallery of PVDF lamella, so these lamella here acted as crosslinking junctions and caused an increase in toughness. The stretched samples showed an α to β transition for the partially miscible blends, whereas there was a weak transition in the miscible blend.

ACKNOWLEDGMENTS

REFERENCES

1. Imken, R. L.; Paul, D. R.; Barlow, J. W. *Polym. Eng. Sci.* **1976**, *9*, 593.

2. Pening, J. P.; Manley, R. S. J. *Macromolecules* **1996**, *29*, 77.

3. Rahman, M. H.; Nandi, A. K. *Macromol. Chem. Phys.* **2002**, *203*, 653.

4. Bernestein, R. E.; Paul, D. R.; Barlow, J. W. *Polym. Eng. Sci.* **1987**, *18*, 1225.

5. Becke, R. E.; Cabasso, I. *Polymer* **1988**, *29*, 1831.

6. Lovinger, A. J. In Developments in Crystalline Polymers; Basset, D. C., Ed.; Elsevier Applied Science: London, **1982**; Vol. *1*.

7. Nishi, T.; Wang, T. T. *Macromolecules* **1977**, *10*, 421.

8. Morra, B. S.; Stein, R. S. *J. Polym. Sci. Part B: Polym. Phys.* **1982**, *20*, 2261.

9. Roerdink, E.; Challa, G. *Polymer* **1978**, *19*, 173.

10. Morra, B. S.; Stein, R. S. *J. Polym. Sci. Part B: Polym. Phys.* **1982**, *20*, 2243.

11. Fatnassi, M.; Larbi, F. B. C.; Dubault, A.; Halary, J. L. *e-Polymer* **2005**, *1*(no. 056).

12. Li, Y.; Oono, Y.; Nakayama, K.; Shimizu, H.; Inoue, T. *Polymer* **2006**, *47*, 3946.

13. Abolhasani, M. M.; Jalali-Arani, A.; Guo, Q.; Nazokdast, H., submitted.

14. Flory, P. J. *J. Chem. Phys.* **1994**, *9*, 660.

15. Flory, P. J. Principles of Polymer Chemistry; Cornell University Press: Ithaca, NY, **1953**.

16. Huggins, M. L. *J. Chem. Phys.* **1941**, *9*, 440.

17. Huggins, M. L. *J. Chem. Phys.* **1942**, *46*, 151.

18. Ruzette, A. V. G.; Mayes, A. M. *Macromolecules* **2001**, *34*, 1907.

19. Ruzette, A. V. G.; Banerjee, P.; Mayes, A. M.; Russell, T. P. *J. Chem. Phys.* **2001**, *114*, 8205.

20. Gonzalez-Leon, A. J.; Mayes, A. M. *Macromolecules* **2001**, *36*, 2508.

21. Mabrouk, K. E.; Bousmina, M. *Rheol. Acta* **2006**, *45*, 959.

22. Gharachorlou, A.; Goharpey, F. *Macromolecules* **2008**, *41*, 3276.

23. Ebert, M.; Garbella, W.; Wendroff, J. *Makromol. Chem. Rapid. Commun.* **1986**, *7*, 65.

24. Ajji, A.; Choplin, L.; Prud'Homme, R. E. *J. Polym. Sci. Part B: Polym. Phys.* **1998**, *26*, 2279.

25. Ajji, A.; Choplin, L.; Prud'Homme, R. E. *J. Polym. Sci. Part B: Polym. Phys.* **1991**, *29*, 1573.

26. Vlassopoulos, D. *Rheol. Acta.* **1996**, *35*, 556.

27. Madbouly, S. A.; Ougizawa, T. *J. Macromol. Sci. Phys.* **2002**, *41*, 255.

28. Madbouly, S. A.; Ougizawa, T. *J. Macromol. Sci. Phys.* **2002**, *41*, 271.

29. Genovese, A.; Shanks, R. A. *Macromol. Mater. Eng.* **2007**, *292*, 184.

30. Fu, Q.; Wang, Y.; Li, Q.; Zhang, G. *Macromol. Mater. Eng.* **2002**, *287*, 397.

31. Ma, P.; Hristova-Bogaerds, D. G.; Lemstra, P. J.; Zhang, Y.; Wang, S. *Macromol. Mater. Eng.* **2012**, *297*, 402.

32. Wu, S. *Polymer* **1985**, *26*, 1855.

33. Bartczak, Z.; Argon, A. S.; Cohen, R. E.; Weinberg, M. *Polymer* **1999**, *40*, 2331.

34. Muratoglu, O. K.; Argon, A. S.; Cohen, R. E.; Weinberg, M. *Polymer* **1995**, *36*, 921.

35. Kayano, Y.; Keskkula, H.; Paul, D. R. *Polymer* **1998**, *39*, 2835.

36. Nele, M.; Soares, J. B. P. *Macromol. Theory Simul.* **2003**, *12*, 386.

37. Yu, Z. Z.; Lei, M.; Ou, Y.; Yang, G. *Polymer* **2000**, *43*, 6993.

38. Vara, R.; Grant, C.; Daniel, C. *World Rubber* **2003**, *227*, 33.

39. (a) Hoffman, J. D.; Weeks, J. J. *J. Chem. Phys.* **1962**, *37*, 1723; (b) Hoffman, J. D.; Weeks, J. J. *J. Res. Natl. Bur. Stand. Sect. A* **1962**, *66*, 13.

40. Lee, J. S.; Kim, K. *J. Fibers Polym.* **2007**, *8*, 237.

41. Briber, R. M.; Khoury, F. *Polymer* **1987**, *28*, 38.

42. Sencadas, V.; Costa, C. M.; Gomez Ribelles, J. L. *J. Mater. Sci.* **2010**, *45*, 1328.

43. Kader, M. A.; Bhowmick, A. K. *Polym. Eng. Sci.* **2003**, *43*, 975.

44. Goh, S. H.; Siow, K. S. *Polym. Bull.* **1988**, *20*, 393.

45. Van Krevelen, D. W.; Hoftyzer, P. J. Properties of Polymers: Correlation with Chemical Structure; Elsevier: New York, **1972**.

46. Bousmina, M.; Lavoie, A.; Riell, B. *Macromolecules* **2002**, *35*, 6774.

47. Ajji, A.; Choplin, L. *Macromolecules* **1991**, *24*, 5221.

48. Fredrickson, G. H.; Larson, R. G. *J. Chem. Phys.* **1987**, *86*, 1553.

49. De Gennes, P. G. Scaling Concept in Polymer Physics; Cornell University Press: Ithaca, NY, **1979**.

50. Friedrich, K. *Adv. Polym. Sci.* **1983**, *52/53*, 225.

51. Magenity, P. M.; Hooper, J. J.; Payneter, C. D.; Riley, A. M.; Nutbeem, C.; Elton, N. J.; Adams, J. M. *Polymer* **1992**, *24*, 5215.

52. Oliveira, M. J.; Cramez, M. C. *J. Macromol. Sci. Phys.* **2001**, *40*, 457.

53. Li, Y.; Oono, Y.; Nakayama, K.; Shimizu, H. *Macromol. Mater. Eng.* **2006**, *291*, 1201.

54. Jiang, Z.; Fu, L.; Sun, Y.; Li, X.; Men, Y. *Macromolecules* **2011**, *44*, 7062.

55. Men, Y.; Strobl, G. *Macromolecules* **2003**, *36*, 1889.

56. Men, Y.; Strobl, G. *Phys. Rev. Lett.* **2003**, *91*, 095502.

57. Li, Y.; Iwakura, Y.; Shimizu, H. *Macromolecules* **2008**, *41*, 33.